Numerical Algorithm of Seismic Wave Propagation and Seismic Attenuation Estimation in Anisotropic Fractured Porous Fluid-Saturated Media

Mikhail Novikov(✉), Vadim Lisitsa, Tatyana Khachkova, Galina Reshetova, and Dmitry Vishnevsky

Sobolev Institute of Mathematics SB RAS,
4 Koptug Avenue, Novosibirsk 630090, Russia
novikovma@ipgg.sbras.ru

Abstract. We present a numerical algorithm of seismic wave propagation in anisotropic fractured fluid-saturated porous media and estimation of seismic attenuation. The algorithm is based on numerical solution of anisotropic Biot equations of poroelasticity. We use finite-difference approximation of Biot equations on the staggered grid. We perform a set of numerical experiments of wave propagation in fractured media. Fractures in the media are connected and filled with anisotropic material providing wave induced fluid flow within connected fractures. Numerical estimations of inverse quality factor demonstrate the effect of fracture-filling material anisotropy on seismic wave attenuation.

Keywords: Biot model · Poroelasticity · Anisotropy · Wave propagation · Seismic attenuation · Inverse quality factor · Finite differences

1 Introduction

On of the most popular research topics in modern geophysics is estimation of reservoir transport properties and fluid mobility. Accurate information about these properties is essential for fractured reservoirs exploration, in particular, CO_2 sequestration [6,15], geothermal energy exploration [12,20]. One of the attributes that can potentially be used as an indicator of transport properties in fractured formations is seismic attenuation. Seismic attenuation in fractured fluid-saturated rock is provided by many essentially different mechanisms. In particular, when a seismic wave propagates through such media, it generates pressure gradients and so cause so-called wave-induced fluid flow (WIFF). Usually these fluid flows are divided in two types. First type is fracture-to-background

The work is supported by Mathematical Center in Akademgorodok, the agreement with Ministry of Science and High Education of the Russian Federation number 075-15-2019-1613.

© Springer Nature Switzerland AG 2021
O. Gervasi et al. (Eds.): ICCSA 2021, LNCS 12949, pp. 434–448, 2021.
https://doi.org/10.1007/978-3-030-86653-2_32

WIFF (FB-WIFF). FB-WIFF is defined mostly by high physical properties contrast between background and fracture-filling material [8,17,19]. Most intense FB-WIFF develops at low frequencies. Conversely, in presence of connected fractures second type of WIFF, fluid flow between fractures (fracture-to-fracture WIFF, FF-WIFF) occurs. In contrast to FB-WIFF, flow of the second type has its intensity maximum at high frequencies. Most important factors affecting FF-WIFF are physical properties of fracture-filling material [5,8,19]. Both types of WIFF result in frequency-dependent seismic wave attenuation. So adequate seismic attenuation estimation can become the base for suggestions about transport properties of the reservoir.

Unfortunately, theoretical studies of WIFF involve relatively simple fracture systems. In particular, studied fracture connectivity is often limited by pairwise intersections of fractures of two orientations [8]. Even if fracture systems are more complex [7] long-distance percolation is not guaranteed. Transport properties of reservoirs depend significantly on the presence of long length chains formed by connected fractures, and it is necessary to study dependencies between fracture connectivity and seismic attenuation. So proper modeling of wave propagation in fractured models with given percolation length is needed to study FF-WIFF and resulting attenuation. Another aspect that must also be taken into consideration is anisotropy. Fracture-filling material should correspond to fracture orientation to provide more realistic fractured media model and obtain more precise correlations between fracture system structure and attenuation.

In this paper, we present a numerical algorithm of seismic wave propagation in anisotropic fractured fluid-saturated porous media and estimation of seismic attenuation. We use presented algorithm to study fracture connectivity effect on seismic attenuation.

2 Anisotropic Biot Equations

Biot theory of poroelasticity is still the most common approach to model seismic waves propagation in porous fluid-saturated media up to the present day in rock physics [2,3,13]. This theory involve two-phase continuous media, where both solid and fluid introduced. Moreover, it involves physical parameters defining the microstructure of the rock and so its transport properties (porosity, tortuosity, permeability) and these parameters can adequately estimated with laboratory experiments for real rocks. In particular, we apply dynamic Biot equations for 2D orthotropic media (in O_{xz} plane) [4]:

$$\rho_f \frac{T_x}{\phi} \frac{\partial q_x}{\partial t} + \frac{\eta}{k_x} q_x = -\frac{\partial p}{\partial x} - \rho_f \frac{\partial v_x}{\partial t} \tag{1}$$

$$\rho_f \frac{T_z}{\phi} \frac{\partial q_z}{\partial t} + \frac{\eta}{k_z} q_z = -\frac{\partial p}{\partial z} - \rho_f \frac{\partial v_z}{\partial t} \tag{2}$$

$$\rho \frac{\partial v_x}{\partial t} = \frac{\partial \sigma_{xx}}{\partial x} + \frac{\partial \sigma_{xz}}{\partial z} - \rho_f \frac{\partial q_x}{\partial t} \tag{3}$$

$$\rho \frac{\partial v_z}{\partial t} = \frac{\partial \sigma_{xz}}{\partial x} + \frac{\partial \sigma_{zz}}{\partial z} - \rho_f \frac{\partial q_z}{\partial t} \tag{4}$$

$$\frac{\partial \sigma_{xx}}{\partial t} = c_{11} \frac{\partial v_x}{\partial x} + c_{13} \frac{\partial v_z}{\partial z} + M\alpha_1 \left(\frac{\partial q_x}{\partial x} + \frac{\partial q_z}{\partial z} \right) \tag{5}$$

$$\frac{\partial \sigma_{zz}}{\partial t} = c_{13} \frac{\partial v_x}{\partial x} + c_{33} \frac{\partial v_z}{\partial z} + M\alpha_3 \left(\frac{\partial q_x}{\partial x} + \frac{\partial q_z}{\partial z} \right) \tag{6}$$

$$\frac{\partial \sigma_{xz}}{\partial t} = c_{55} \left(\frac{\partial v_z}{\partial x} + \frac{\partial v_x}{\partial z} \right) \tag{7}$$

$$-\frac{\partial p}{\partial t} = M\alpha_1 \frac{\partial v_x}{\partial x} + M\alpha_3 \frac{\partial v_z}{\partial z} + M \left(\frac{\partial q_x}{\partial x} + \frac{\partial q_z}{\partial z} \right) \tag{8}$$

Biot model describes solid particles velocity (v_x v_z) and relative fluid velocity (q_x q_z), as well as stress tensor components σ_{xx}, σ_{zz}, σ_{xz}, and fluid pressure p. Here ρ_f is the fluid density, η is fluid viscosity, ρ is the density of saturated material. Parameters T_x, T_z and k_x, k_z represent anisotropic tortuosity and permeability components for x-axis and z-axis directions, respectively. Equations also include undrained material modulus tensor components c_{ij}, fluid-solid coupling modulus M (also known as fluid storage coefficient) and Biot effective stress components α_x, α_z (Biot-Willis constants).

3 Numerical Scheme

To perform numerical experiments we present explicit second order finite-difference scheme approximating equations (1–8) on the staggered grid [23], where different fields components are defined in different nodes (Fig. 1). Let i, j, n be integer and correspond to grid node indices in x- and z-direction and number of time step, respectively. Then normal stresses σ_{xx} and σ_{zz}, are stored in nodes $(i\Delta x, j\Delta z, (n+1/2)\Delta t)$. Fluid and solid velocities x-components v_x, q_x are stored in nodes $((i+1/2)\Delta x, j\Delta z, n\Delta t)$, and z-components are defined in nodes $(i\Delta x, (j+1/2)\Delta z, n\Delta t)$. Shear stress σ_{zz} is stored in nodes $((i+1/2)\Delta x, (j+1/2)j\Delta z, (n+1/2)\Delta t)$. Note that physical parameters of the media are stored in nodes $(i\Delta x, j\Delta z)$ and need to be properly averaged in following equations.

Therefore we approximate equations (1–8) by the system of finite-difference equations

$$\begin{aligned} D_t[q_x]^{n-\frac{1}{2}}_{i+\frac{1}{2}j} &= (C_1)_{i+1/2j} \left(D_x[\sigma_{xx}]^{n-\frac{1}{2}}_{i+\frac{1}{2}j} + D_z[\sigma_{xz}]^{n-\frac{1}{2}}_{i+\frac{1}{2}j} \right) \\ &+ (C_2)_{i+1/2j} D_x[p]^{n-\frac{1}{2}}_{i+\frac{1}{2}j} + A_x \left[\frac{\eta}{k_x} \right]^{n-1/2}_{i+1/2j} C_2 A_t[q_x]^{n-1/2}_{i+1/2j}, \end{aligned} \tag{9}$$

$$\begin{aligned} D_t[q_z]^{n-\frac{1}{2}}_{ij+\frac{1}{2}} &= (C_3)_{i+j1/2} \left(D_x[\sigma_{xz}]^{n-\frac{1}{2}}_{ij+\frac{1}{2}} + D_z[\sigma_{zz}]^{n-\frac{1}{2}}_{ij+\frac{1}{2}} \right) \\ &+ (C_4)_{i+j1/2} D_z[p]^{n-\frac{1}{2}}_{ij+\frac{1}{2}} + A_z \left[\frac{\eta}{k_z} \right]^{n-\frac{1}{2}}_{ij+\frac{1}{2}} C_4 A_t[q_z]^{n-\frac{1}{2}}_{ij+\frac{1}{2}}, \end{aligned} \tag{10}$$

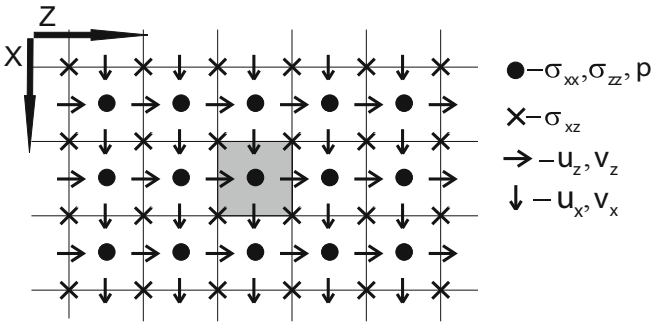

Fig. 1. Schematic illustration of staggered grid.

$$D_t[v_x]^{n-\frac{1}{2}}_{i+\frac{1}{2}j} = (C_5)_{i+1/2j}\left(D_x[\sigma_{xx}]^{n-\frac{1}{2}}_{i+\frac{1}{2}j} + D_z[\sigma_{xz}]^{n-\frac{1}{2}}_{i+\frac{1}{2}j}\right) - (C_1)_{i+1/2j} D_x[p]^{n-\frac{1}{2}}_{i+\frac{1}{2}j} - A_x\left[\frac{\eta}{k_x}\right]^{n-1/2}_{i+1/2j} C_1 A_t[q_x]^{n-1/2}_{i+1/2j}, \tag{11}$$

$$D_t[v_z]^{n-\frac{1}{2}}_{ij+\frac{1}{2}} = (C_6)_{i+j1/2}\left(D_x[\sigma_{xz}]^{n-\frac{1}{2}}_{ij+\frac{1}{2}} + D_z[\sigma_{zz}]^{n-\frac{1}{2}}_{ij+\frac{1}{2}}\right) - (C_3)_{i+j1/2} D_z[p]^{n-\frac{1}{2}}_{ij+\frac{1}{2}} - A_z\left[\frac{\eta}{k_z}\right]^{n-\frac{1}{2}}_{ij+\frac{1}{2}} C_3 A_t[q_z]^{n-\frac{1}{2}}_{ij+\frac{1}{2}}, \tag{12}$$

$$D_t[\sigma_{xx}]^n_{ij} = (c^u_{11})_{ij} D_x[v_x]^n_{ij} + (c^u_{13})_{ij} D_z[v_z]^n_{ij} + (\alpha_1)_{ij} M_{ij}(D_x[q_x]^n_{ij} + D_z[q_z]^n_{ij}), \tag{13}$$

$$D_t[\sigma_{zz}]^n_{ij} = (c^u_{13})_{ij} D_x[v_x]^n_{ij} + (C^u_{33})_{ij} D_z[v_z]^n_{ij} + (\alpha_3)_{ij} M_{ij}(D_x[q_x]^n_{ij} + D_z[q_z]^n_{ij}), \tag{14}$$

$$D_t[\sigma_{xz}]^n_{i+\frac{1}{2}j+\frac{1}{2}} = (\tilde{c}^u_{55})_{i+1/2j+1/2}(D_z[v_x]^n_{i+\frac{1}{2}j+\frac{1}{2}} + D_x[v_z]^n_{i+\frac{1}{2}j+\frac{1}{2}}), \tag{15}$$

$$D_t[p]^n_{ij} = -\alpha_{ij} M_{ij}(D_x[v_x]^n_{ij} + D_z[v_z]^n_{ij}) + M_{ij}(D_x[q_x]^n_{ij} + D_z[q_z]^n_{ij}), \tag{16}$$

where D_x, D_z and D_t - second order central difference operators, and operators A_x and A_z represent spatial averaging in x- and z-axis, respectively. Operator A_t is time averaging. For discontinuous coefficients we apply the volume balance technique [21] to obtain the second order of convergence of numerical solution in models with sharp interfaces aligned to the grid lines [9,16]. So use following notations for coefficients:

$$
\begin{aligned}
(C_1^{-1})_{i+1/2j} &= A_x[\rho_f]_{i+1/2j} - \frac{A_x[\rho]_{i+1/2j} A_x[T_x]_{i+1/2j}}{A_x[\phi]_{i+1/2j}}, \\
(C_2^{-1})_{i+1/2j} &= \frac{\left(A_x[\rho_f]_{i+1/2j}\right)^2}{A_x[\rho]_{i+1/2j}} - \frac{A_x[\rho_f]_{i+1/2j} A_x[T_x]_{i+1/2j}}{A_x[\phi]_{i+1/2j}}, \\
(C_3^{-1})_{ij+1/2} &= A_z[\rho_f]_{ij+1/2} - \frac{A_z[\rho]_{ij+1/2} A_z[T_z]_{ij+1/2}}{A_z[\phi]_{ij+1/2}}, \\
(C_4^{-1})_{ij+1/2} &= \frac{\left(A_z[\rho_f]_{ij+1/2}\right)^2}{A_z[\rho]_{ij+1/2}} - \frac{A_z[\rho_f]_{ij+1/2} A_z[T_z]_{ij+1/2}}{A_z[\phi]_{ij+1/2}}, \\
(C_5^{-1})_{i+1/2j} &= A_x[\rho]_{i+1/2j} - \frac{A_x[\rho_f]_{i+1/2j} A_x[\phi]_{i+1/2j}}{A_x[T_x]_{i+1/2j}}, \\
(C_6^{-1})_{ij+1/2} &= A_z[\rho]_{ij+1/2} - \frac{A_z[\rho_f]_{ij+1/2} A_z[\phi]_{ij+1/2}}{A_z[T_z]_{ij+1/2}}.
\end{aligned}
\tag{17}
$$

Finally, to average undrained stiffness tensor component c_{55} in nodes $((i+1/2)\Delta x, (j+1/2)\Delta z)$ we apply the formula of the harmonic mean:

$$
(\tilde{c}_{55}^u)^{-1}_{i+1/2j+1/2} = \frac{1}{4}\left(\frac{1}{(c_{55}^u)_{ij}} + \frac{1}{(c_{55}^u)_{i+1j}} + \frac{1}{(c_{55}^u)_{ij+1}} + \frac{1}{(c_{55}^u)_{i+1j+1}}\right).
$$

4 Problem Set Up

We apply numerical modeling of plane P-wave propagation within fractured porous fluid-saturated media. As a computational domain we consider rectangular area of poroelastic medium (Fig. 2). This medium consists of homogeneous background containing inhomogeneous layer, where heterogeneities are presented by the fractures filled with more permeable highly porous material to provide the flow of fluid. The signal is propagated in z-direction through fractured layer of interest and also through two receiver lines located at both sides of it. Thus, we record the wave before and after its interaction with the fractured layer.

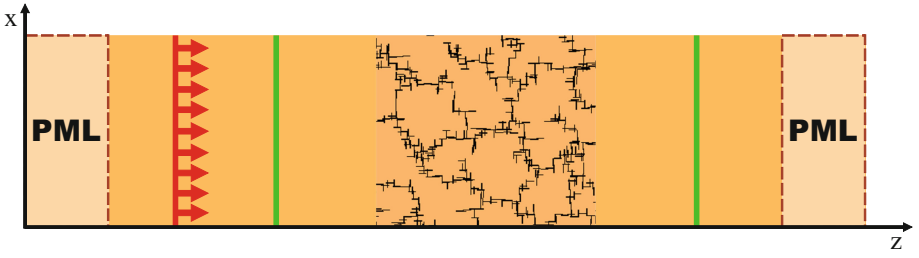

Fig. 2. A sketch of the computational domain and the acquisition system. Red line correspond to the source positions and wave propagation direction, two green lines represent the receiver positions (Color figure online).

The size of computational domain in x-direction is 1 m, and z-direction size L_z vary depending on the signal wavelength. At the boundaries $x = 0$ m and $x = 1$ m we impose periodic conditions, and perfectly matched layers [1,10,11] are set at two other boundaries $z = 0$ m and $z = L_z$ m. Grid step in both directions is $\Delta x = \Delta z = 2$ mm.

5 Numerical Estimation of Seismic Attenuation

As we want to observe correlation between fracture connectivity and seismic attenuation, proper estimation should be calculated for parameter characterizing this attenuation. Standard parameter demonstrating wave attenuation is inversed quality factor, and it can be calculated by many techniques [14]. One approach to calculate the inverse quality factor is using complex frequency-dependent phase velocity of seismic wave $c(\omega)$:

$$Q^{-1} = \frac{\Im(c(\omega))}{\Re(c(\omega))}. \tag{18}$$

Having recorded signals from numerical modeling of wave propagation in media of interest, it is convenient to apply spectral ratio method to estimate total attenuation.

To estimate inverse quality factor we consider a plane wave propagating in z-direction through the fractured domain

$$v(t,z) = v_0 e^{i\omega(t-z/c(\omega))} = v_0 e^{i\omega(t-zs(\omega))}, \tag{19}$$

where $c(\omega)$ is the complex frequency-dependent effective phase velocity of the medium, and $s(\omega) = 1/c(\omega)$ is the slowness. During wave propagation, wave amplitude v_0 is changing due to attenuation within the fractured media. Assume that first receiver line is located in $z = z_1$. Then the average (in x-direction) of the recorded signal in first receiver line is given by

$$\langle v(t,x,z_1)\rangle_x = v_1 = v_0 e^{i\omega(t-z_1 s(\omega))}. \tag{20}$$

In our numerical experiments, domain between two receiver lines contains three layers - two homogeneous layers on either side of third, fractured layer. So, first, it is necessary to take into account transmission losses in two homogeneous layers. Let us denote size in z-direction for left homogeneous layer, fractured layer, and right homogeneous layer by l_1, L_f and l_2, respectively, and also denote the slowness within background media by $s_b(\omega)$. Then we can represent averaged signal recorded in second receiver line

$$\langle v(t,x,z_2)\rangle_x = v_2 = v_0 e^{i\omega(t-z_1 s(\omega))} e^{-i\omega(l_1+l_2)s_b(\omega)} e^{-i\omega L_f s_f(\omega)}, \tag{21}$$

where $s_f(\omega)$ is effective slowness in fractured layer.
Let us denote factor representing wave propagation in homogeneous background by v_b, so

$$\langle v(t,x,z_2)\rangle_x = v_2 = v_1 v_b e^{-i\omega L_f \Re(s_f(\omega))} e^{\omega L_f \Im(s_f(\omega))}. \tag{22}$$

Hence we obtain the imaginary part of effective slowness in the layer of interest as follows:

$$\Im(s_f(\omega)) = \frac{1}{\omega L_f} ln \left| \frac{v_2}{v_1 v_b} \right|. \tag{23}$$

However, the real part of $s(\omega)$ is many-valued, and to determine the phase uniquely, we use the approximation of phase velocity in fractured layer. We pick the travel times t_1 and t_2 at the maximum amplitude of the two signals for the two receiver positions, and, since we know the background velocity, we can approximate phase velocity within the fractured layer by

$$V_P^0 = \frac{L_f}{t_2 - t_1 - t_b}, \tag{24}$$

where $t_b = (l_1 + l_2)/\Re(v_b)$ is the time of wave propagation in two homogeneous layers between the receiver lines. Therefore, the phase $\Re(s_f)$ is chosen to satisfy the condition

$$\left| \frac{\Re(s_f)}{\omega L_f} - \frac{\omega L_f}{V_P^0} \right| < \pi. \tag{25}$$

However, some error in attenuation estimation can be also associated with the fact that the fractured layer is finite. Moreover, the set up of experiment causes reflections on interfaces between homogeneous and fractured layer. To avoid these effects, consider two numerical experiments, where fractured layer lengths L_f and L'_f are different. Also assume that considered error is presented by the factor $e^{-i\phi(\omega)}$ (regardless of layer length) in the signal expression, so we have

$$\begin{aligned} v_2 &= v_1 v_b e^{-i\omega(L_f \Re(s_f(\omega)) + \Re(\phi)/\omega)} e^{\omega(L_f \Im(s_f(\omega)) + \Im(\phi)/\omega)}, \\ v'_2 &= v_1 v_b e^{-i\omega(L'_f \Re(s_f(\omega)) + \Re(\phi)/\omega)} e^{\omega(L'_f \Im(s_f(\omega)) + \Im(\phi)/\omega)} \end{aligned} \tag{26}$$

for the averaged signals recorded in second receiver line for first and second experiment, correspondingly. Set these new signal representations equal to ones analogous to (21)

$$v_2 = v_0 e^{i\omega(t - z_1 s(\omega))} e^{-i\omega(l_1+l_2)s_b(\omega)} e^{-i\omega L_f \hat{s}_f(\omega)}, \tag{27}$$

$$v'_2 = v_0 e^{i\omega(t - z_1 s(\omega))} e^{-i\omega(l_1+l_2)s_b(\omega)} e^{-i\omega L'_f \hat{s}'_f(\omega)}, \tag{28}$$

where $\hat{s}_f$ and $\hat{s}'_f$ are two known different slowness estimations for two experiments. As a result, we obtain a system of two equations for our new estimation for imaginary part of the slowness

$$\Im(s_f(\omega)) + \frac{\Im(\phi(\omega))}{\omega L_f} = \Im(\hat{s_f}), \tag{29}$$

$$\Im(s_f(\omega)) + \frac{\Im(\phi(\omega))}{\omega L'_f} = \Im(\hat{s_f}'), \tag{30}$$

and its real part

$$\Re(s_f(\omega)) + \frac{\Re(\phi(\omega))}{\omega L_f} = \Re(\hat{s_f}), \tag{31}$$

$$\Re(s_f(\omega)) + \frac{\Re(\phi(\omega))}{\omega L'_f} = \Re(\hat{s_f}'). \tag{32}$$

Obviously, in such case we can obtain exact solution for $s_f(\omega)$, and then estimate inverse quality factor using formula (18). However, in case of three and more signals propagated in fractured layers of different length, one may apply, for example, least squares method to retrieve complex slowness.

6 Numerical Experiments

First we perform numerical experiments to verify the proposed attenuation estimation method. We model the propagation of seismic wave through homogeneous anisotropic layer located in more stiff and less porous and permeable background. For the fluid we set density $\rho_f = 1090$ kg/m^3, and fluid viscosity $\eta = 0.001$ Pa·s. Other physical properties of both materials are given in Table 1. We perform two sets experiments for two different lengths of anisotropic layer of interest $L = d$ and $L = 0.5d$, where d is approximately four wavelengths in the background.

Resulting numerical estimations of inverse quality factor and phase velocity are presented in Fig. 3. We can clearly observe that lesser length of the layer provide bigger error in comparison with both bigger length and analytical solution, which is obtained from dispersion relation of Biot model (1–8). However, applying our method described in Subsect. 5 results in more precise estimations, what is observed in better agreement with analytical estimations, especially for inverse quality factor. Note that although our numerical Q^{-1} estimation relative error (in comparison with analytical one) for worst case ($L = d$) at some frequencies almost reach 1, we observe good agreement of all velocity estimations with relative error less than 10^{-3}.

Next we perform a set of numerical experiments to study the anisotropy effect on seismic attenuation. We apply discrete fracture networks formed by two sets of microscale fractures parallel to x-axis and z-axis. Fractures are represented by rectangulars with length 30 mm and width 4 mm. Moreover, fracture systems are generated by simulated annealing approach [22,24] to provide given distance, that can be traveled within continuous chain of fractures throughout the fractured model. In other words, we consider models with different connectivity degree. Fracture network generation process is described in detail in [18], and examples of models of different connectivity degrees are demonstrated in Fig. 4. We consider homogeneous isotropic extremely low permeable media as the background (physical properties are provided in the first column in Table 2),

Table 1. Material properties.

Parameter	Background	Homogeneous layer
Drained rock		
Porosity ϕ	0.1	0.3
x-axis Permeability k_x, m^2	10^{-13}	5^{-10}
z-axis Permeability k_z, m^2	10^{-13}	$2 \cdot 10^{-13}$
x-axis Tortuosity T_x	1.83	2.2
z-axis Tortuosity T_z	1.83	3.29
x-axis Biot and Willis constant α_1	0.2962	0.6759
z-axis Biot and Willis constant α_3	0.2962	0.9991
Undrained rock		
Density ρ, kg/m^3	2494	2182
Undrained modulus c_{11}, GPa	69.1	36.59
Undrained modulus c_{33}, GPa	69.1	6.885
Undrained modulus c_{13}, GPa	7.159	4.629
Undrained modulus c_{55}, GPa	31	0.02
Fluid storage coefficient M, GPa	20.102	6.8304

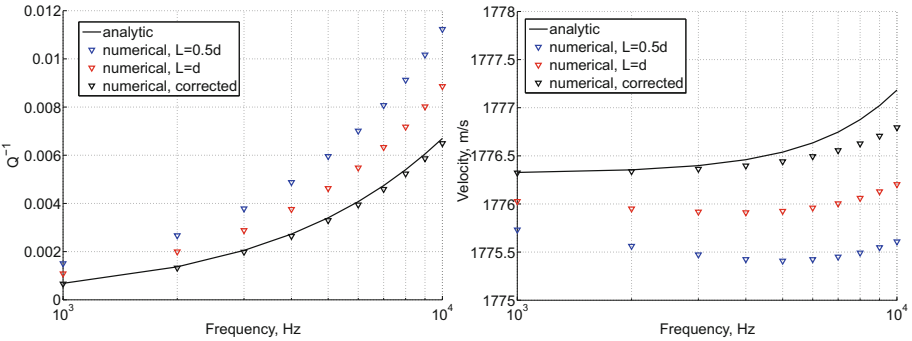

Fig. 3. Inverse quality factor (left) and phase velocity (right) for homogeneous anisotropic layer.

and fractures are filled with anisotropic material. Moreover, to intensify fluid flow within fractures along fractures of both orientation, we set proper physical parameters for x-axis oriented fractures, z-axis oriented fractures and its intersections. In particular, we set bigger permeability, smaller tortuosity and reduce stiffness of the material in fracture direction. Physical properties of fracture-filling materials for x-axis oriented fractures, z-axis oriented fractures and intersections of fractures of two different orientations are given in second, third, and

fourth columns in Table 2, respectively. Fluid density is 1000 kg/m^3, and fluid viscosity is 0.001 Pa·s. Numerical experiments of wave propagation are performed for fractured models of six different degrees of connectivity (10 realizations for each case) and for 1–10 kHz initial signal central frequency range.

Table 2. Fractured media materials

Parameter	BG	FX	FZ	FXZ	ISO1	ISO2
Drained rock						
Porosity ϕ	0.1	0.225	0.225	0.225	0.2250	0.1425
x-axis Permeability k_x, m^2	10^{-15}	$1.414 \cdot 10^{-10}$	$5.3 \cdot 10^{-13}$	$1.414 \cdot 10^{-10}$	$1.414 \cdot 10^{-10}$	$5.3 \cdot 10^{-13}$
z-axis Permeability k_z, m^2	10^{-15}	$5.3 \cdot 10^{-13}$	$1.414 \cdot 10^{-10}$	$1.414 \cdot 10^{-10}$	$1.414 \cdot 10^{-10}$	$5.3 \cdot 10^{-13}$
x-axis Tortuosity T_x	1.83	1.17	1.83	1.17	1.17	1.83
z-axis Tortuosity T_z	1.83	1.83	1.17	1.17	1.17	1.83
x-axis Biot and Willis constant α_1	0.2962	0.6896	0.6418	0.6915	0.7346	0.7346
z-axis Biot and Willis constant α_3	0.2962	0.6418	0.6896	0.6915	0.7346	0.7346
Undrained rock						
Density ρ, kg/m^3	2494	1870	2458	2318	2318	2318
Undrained modulus c_{11}, GPa	69.097	38.958	46.432	38.958	38.958	46.432
Undrained modulus c_{33}, GPa	69.097	46.432	38.958	38.958	38.958	46.432
Undrained modulus c_{13}, GPa	7.159	19.811	19.811	19.811	16.337	23.81
Undrained modulus c_{55}, GPa	30.969	11.311	11.311	11.311	11.311	11.311
Fluid storage coefficient M, GPa	20.1	9.4287	9.4287	9.4026	9.33	9.488

Resulting fluid pressure field snapshots for six fractured media models with different connectivity degree are demonstrated in Fig. 5. As background permeability is very low, fluid flow in fractures is induced by pressure contrasts at the background/fracture interfaces. So, we observe intensive pressure gradients behind propagated wave only within the connected fractures. Moreover, pressure gradients increase more intensively when fracture connectivity is relatively low (snapshots A, B and C in Fig. 5). Difference in pressure gradients in fracture systems with high connectivity are almost unobservable.

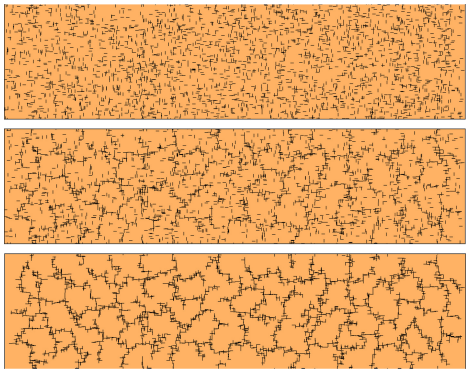

Fig. 4. Models of fractured media with different percolation length (increasing from top to bottom).

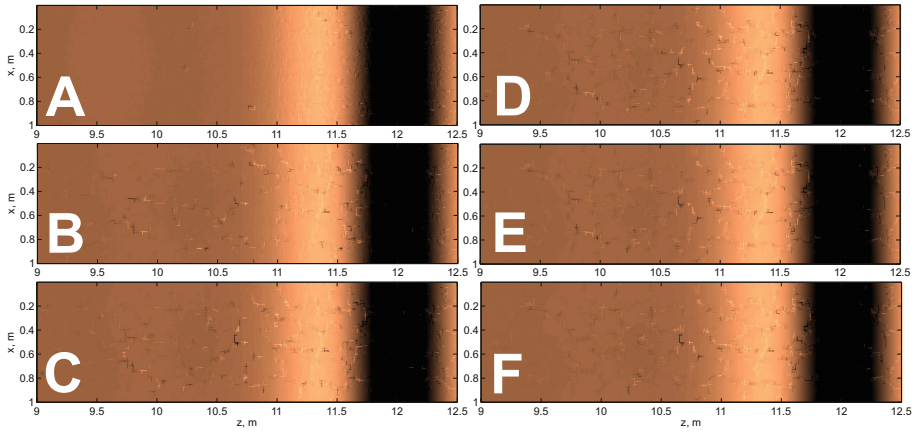

Fig. 5. Fluid pressure in fractured media with different percolation (percolation length increases from A to F). Signal central frequency is 3 kHz.

To study anisotropy effect on seismic attenuation we also perform a set of numerical experiments considering isotropic fracture-filling material. All fractured media models are the same as described above except physical properties for material in fractures. We consider two models of material. First model is soft and have high permeability (similar to properties along the fractures in previous experiments) in both axis directions (fifth column in Table 2). In contrast, second model represent stiff and low permeable isotropic material with lower porosity (sixth column in Table 2).

To compare two isotropic fracture-filling materials we demonstrate fluid pressure field snapshots in Fig. 6 for almost not connected fractures and higher connectivity considered. In soft material case pressure gradients within fractures can be easily observed. However, stiff material provide almost no pressure gradients. Additionally, we again observe higher pressure gradients for high fracture connectivity, at least for soft material in fractures.

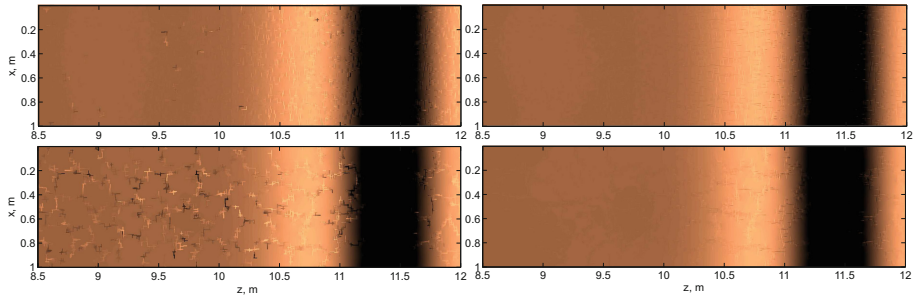

Fig. 6. Fluid pressure in isotropic fractured media. Top images correspond to the lowest fracture connectivity, bottom images represent results for the highest fracture connectivity; row correspond to fracture-filling material: left - soft, right - stiff. Signal central frequency is 3 kHz.

Finally, we estimate wave attenuation for all three fracture-filling materials and all six degrees of connectivity. Obtained frequency-dependent inverse quality factor estimates are presented in Fig. 7. First, we observe the increase of attenuation with fracture connectivity increase. Also attenuation predictably increases with frequency increase in general, and attenuation peak for all cases at the frequency near to 5 kHz can be caused by fractured model periodicity. Additionally, we see that most significant increase of attenuation occurs from almost non-intersecting fractures to first two considered connectivity stages. Furthermore, the highest values of Q^{-1} are obtained in case of isotropic soft material for almost all frequencies and connectivity degrees. Estimations for isotropic stiff fracture-filling material are generally smaller than other estimations, except the case of non-intersecting fractures. Such effect is probably observed because with negligible wave induced fluid flow (both between fractures and background and within fractures) scattering is the only significant attenuation mechanism, which is independent of permeability. As expected, attenuation in the case of anisotropy almost always stays in range limited by attenuation for isotropic stiff material from below and by attenuation for isotropic soft material from above. However, attenuation observably differs between anisotropic and isotropic fracture filler. Thus it is important to take into account the anisotropy of material providing fluid transport in fractured porous fluid-saturated media.

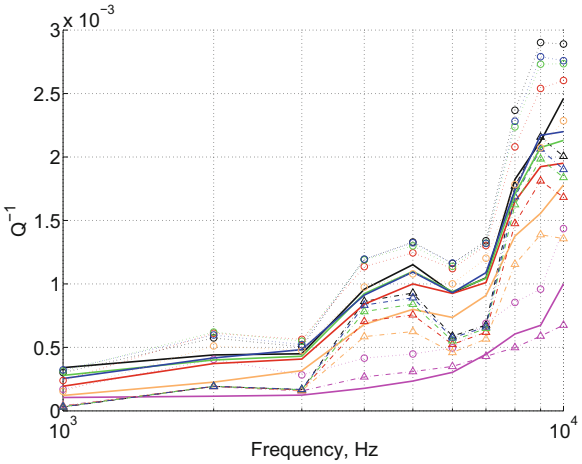

Fig. 7. Inverse quality factor for fractured media. Line style corresponds to fracture-filling material: thick solid lines - anisotropic, dashed lines with circles - isotropic soft, dash-and-dot lines with triangles - isotropic stiff. Colors correspond to fracture connectivity degrees in increasing order: pink, yellow, red, green, blue, black (Color figure online)

7 Conclusion

In our work we present a numerical algorithm of seismic wave propagation in anisotropic fractured porous fluid-saturated media and estimate wave attenuation in such media. The algorithm is based on numerical solution of Biot equations of poroelasticity using staggered-grid finite-difference scheme. Seismic attenuation estimation is provided by inverse quality factor calculation based on spectral ratio approach. Presented algorithm is used to study the effect of fracture-filling material anisotropy and fracture connectivity on seismic wave attenuation. We numerically model wave propagation through fractured media with complex two-scale structure in frequency range from 1 to 10 kHz. Numerical experiments include different degrees of fracture connectivity as well as fracture-filling material properties. We consider anisotropic material in fractures providing better transport properties along the fractures than transversely to fractures. Results show that both fracture connectivity and anisotropy significantly affects seismic wave attenuation.

References

1. Berenger, J.P.: A perfectly matched layer for the absorption of electromagnetic waves. J. Comput. Phys. **114**(2), 185–200 (1994)
2. Biot, M.A.: Theory of propagation of elastic waves in fluid-saturated porous solid. I. Low-frequency range. J. Acoust. Soc. Am. **28**, 168–178 (1956)

3. Carcione, J.M., Morency, C., Santos, J.E.: Computational poroelasticity – a review. Geophysics **75**(5), 75A229–75A243 (2010)
4. Cheng, A.H.D.: Material coefficients of anisotropic poroelasticity. Int. J. Rock Mech. Min. Sci. **342**, 199–205 (1997)
5. Guo, J., Rubino, J.G., Glubokovskikh, S., Gurevich, B.: Effects of fracture intersections on seismic dispersion: theoretical predictions versus numerical simulations. Geophys. Prospect. **65**(5), 1264–1276 (2017)
6. Huang, F., et al.: The first post-injection seismic monitor survey at the Ketzin pilot CO_2 storage site: results from time-lapse analysis. Geophysical Prospect. **66**(1), 62–84 (2018)
7. Hunziker, J., et al.: Seismic attenuation and stiffness modulus dispersion in porous rocks containing stochastic fracture networks. J. Geophys. Res. Solid Earth **123**(1), 125–143 (2018)
8. Kong, L., Gurevich, B., Zhang, Y., Wang, Y.: Effect of fracture fill on frequency-dependent anisotropy of fractured porous rocks. Geophys. Prospect. **65**(6), 1649–1661 (2017)
9. Lisitsa, V., Podgornova, O., Tcheverda, V.: On the interface error analysis for finite difference wave simulation. Comput. Geosci. **14**(4), 769–778 (2010)
10. Lisitsa, V.: Optimal discretization of PML for elasticity problems. Electron. Trans. Numer. Anal. **30**, 258–277 (2008)
11. Martin, R., Komatitsch, D., Ezziani, A.: An unsplit convolutional perfectly matched layer improved at grazing incidence for seismic wave propagation in poroelastic media. Geophysics **73**(4), T51–T61 (2008)
12. Marty, N.C.M., Hamm, V., Castillo, C., Thiery, D., Kervevan, C.: Modelling water-rock interactions due to long-term cooled-brine reinjection in the dogger carbonate aquifer (paris basin) based on in-situ geothermal well data. Geothermics **88**, 101899 (2020)
13. Masson, Y.J., Pride, S.R.: Finite-difference modeling of Biot's poroelastic equations across all frequencies. Geophysics **75**(2), N33–N41 (2010)
14. Mavko, G., Mukerj, T., Dvorkin, J.: The Rock Physics Handbook, 2nd edn. Cambridge University Press, Cambridge (1999)
15. Menke, H.P., Reynolds, C.A., Andrew, M.G., Pereira Nunes, J.P., Bijeljic, B., Blunt, M.J.: 4D multi-scale imaging of reactive flow in carbonates: assessing the impact of heterogeneity on dissolution regimes using streamlines at multiple length scales. Chem. Geol. **481**, 23–37 (2018)
16. Moczo, P., Kristek, J., Galis, M.: The Finite-Difference Modelling of Earthquake Motion: Waves and Ruptures. Cambridge University Press, Cambridge (2014)
17. Muller, T.M., Gurevich, B., Lebedev, M.: Seismic wave attenuation and dispersion resulting from wave-induced flow in porous rocks – a review. Geophysics **75**(5), 75A147–75A164 (2010)
18. Novikov, M.A., Lisitsa, V.V., Bazaikin, Y.V.: Wave propagation in fractured porous media with different percolation length of fracture systems. Lobachevskii J. Math. **41**(8), 1533–1544 (2020)
19. Rubino, J.G., Muller, T.M., Guarracino, L., Milani, M., Holliger, K.: Seismoacoustic signatures of fracture connectivity. J. Geophys. Res. Solid Earth **119**(3), 2252–2271 (2014)
20. Salaun, N., et al.: High-resolution 3D seismic imaging and refined velocity model building improve the image of a deep geothermal reservoir in the Upper Rhine Graben. Lead. Edge **39**(12), 857–863 (2020)
21. Samarskii, A.A.: The Theory of Difference Schemes. (Pure and Applied Mathematics), vol. 240. CRC Press, Bosa Roca (2001)

22. Tran, N.: Simulated annealing technique in discrete fracture network inversion: optimizing the optimization. Comput. Geosci. **11**, 249–260 (2007)
23. Virieux, J.: P-SV wave propagation in heterogeneous media: velocity-stress finite-difference method. Geophysics **51**(4), 889–901 (1986)
24. Xu, C., Dowd, P.: A new computer code for discrete fracture network modelling. Comput. Geosci. **36**(3), 292–301 (2010)